

Aerodynamic Analysis of Transonic Manoeuvre Devices Using an Unstructured-Grid, Navier-Stokes Flow Solver

L. J. Johnston

University of Salford, School of Computing, Science and Engineering

Salford, Greater Manchester, M5 4WT, United Kingdom

Email: l.j.johnston@salford.ac.uk

Abstract

The viscous, transonic flow development around the SKF 1.1 supercritical aerofoil section, in clean configuration and equipped with either a trailing-edge flap or a leading-edge slat, is computed using an unstructured-grid based flow solver for the Reynolds-averaged Navier-Stokes equations. A full differential Reynolds-stress turbulence model is employed in the computations to model the Reynolds stresses appearing in the mean-flow equations. The wall-function approach is adopted to bridge the molecular-viscosity dominated region immediately adjacent to solid boundaries. Predicted surface pressure distributions are compared with experimental data, for a free-stream Mach number of 0.6 and a range of incidence angles, and generally show a satisfactory level of agreement. There are some discrepancies in the region of the upper surface shock wave/boundary layer interactions that are probably partially due to uncertainties in the wind-tunnel wall interference corrections to be applied to the experimental data. However, the influence of the near-wall treatment in the computations also requires further investigation.

1. Introduction

Mechanical high-lift systems, comprising trailing-edge flaps and possibly leading-edge slats, are used by most aircraft during the take-off and landing phases of flight. Flaps provide additional lift at low speed beyond that provided by the clean wing configuration of the aircraft, and slats enable higher incidence angles to be attained before significant upper surface flow separation takes place. The high-lift system can have a significant impact on the overall aerodynamic characteristics of the aircraft, with small improvements in the high-lift efficiency of the wing leading to significant gains in payload, field length and climb-out performance^{1,2}. For combat aircraft, Figure 1, there is an additional requirement that the wing must be able to generate high lift at transonic flow conditions, in order to enhance manoeuvring performance, without incurring an excessive drag penalty or promoting the onset of shock-induced flow separation or buffet. The use of supercritical aerofoil sections on the clean wing planform can help in this regard by allowing rearward movement of upper-surface shock waves without an increase in shock-wave strength. Flight tests of an F-4E Phantom II aircraft equipped with leading-edge slats³ have demonstrated significantly-improved climb and turn manoeuvrability, even without complete optimisation of the slat configuration. Whitford⁴ provides an example of such an improvement with the aircraft in a steady-state turn at a flight Mach number of 0.6 and an altitude of 10,000 ft. The aircraft can execute a 180° turn in 14.2 seconds at a load factor of 4.5g when equipped with slats, compared with 19.0 seconds at a load factor of 3.5g without slats. However, the aerodynamic benefits of high-lift systems need to be balanced against the weight penalty and additional system complexity.

The additional lift generated by deployment of a high-lift system is achieved by the increased effective camber and chord-wise extent of the multi-element wing planform. Such a wing is generally able to operate at higher incidence angles since the upper surface pressure rise to the trailing edge is split over a number of wing elements. The multi-element nature of the geometry leads to the presence of more complex flow phenomena such as turbulent wake/boundary layer mixing and closed re-circulation bubbles in flap and slat cove regions, Figure 2. Also, the wakes of upstream geometry elements develop in the stream-wise adverse pressure gradients of the downstream geometry elements which can result in off-the-surface flow-reversal in the wake. Finally, at transonic manoeuvring conditions there are likely to be shock waves present on the main wing element and possibly also on the flaps and/or slats. The viscous flow development through the gap regions between the main wing and the flap and slat elements

means that optimisation of the high-lift geometry, in terms of gaps, overlaps and angles, is significantly Reynolds number dependent. Thus, the results of optimisation studies using wind tunnel testing of sub-scale models at lower Reynolds numbers can be difficult to extrapolate to flight conditions. It is in this area, particularly, that Computational Fluid Dynamics (CFD) methods can give some insight and so complement wind tunnel test programmes.

Nield⁵ considers the high-lift design process for low-speed applications, highlighting the importance of modern CFD methods which are able to provide predictions of aerodynamic performance at flight Reynolds numbers. The quantitative accuracy of these CFD methods is very dependent upon the validity of the engineering turbulence models used to approximate the physics in the governing mean-flow equations. The development and application of CFD methods to transonic, high-lift flow conditions has received much less attention than the low-speed, take-off and landing flight regime. Inviscid-flow methods for two-element aerofoil configurations were developed in the mid 1970s, with Caughey⁶ using the transonic small-disturbance equations for example. Grossman and Melnik⁷ and Arlinger⁸ solved the full-potential equation, using conformal mapping techniques to transform the flow around a two-element aerofoil into the annular region between two concentric circles. Rosch and Klevenhusen⁹ developed a method applicable to more general multi-element aerofoil geometries by using computational grids consisting of the streamlines and equi-potential lines of the incompressible flow-field around the geometry. Initial attempts to develop viscous flow methods involved the coupling of boundary-layer methods to the inviscid flow solvers; see Grossman and Volpe¹⁰, Leicher¹¹ and Rosch and Klevenhusen⁹. Such viscous/inviscid coupled methods tend to break down with the onset of flow separation, limiting their practical use in the design process. The use of modern CFD methods, based around solutions of the Reynolds-averaged Navier-Stokes equations, provide a more practical basis for a high-lift analysis method. Rumsey and Ying¹² review methods developed for application to low-speed, high-lift flows, the majority of the methods being based on structured-grid formulations and employing the turbulent-viscosity approach to model the Reynolds stresses appearing in the mean-flow equations. Stolcis and Johnston¹³ describe the initial application of an unstructured-grid, Navier-Stokes flow solver and the k- ϵ turbulence model to an aerofoil equipped with a trailing-edge flap at transonic flow conditions.

2. Computational Method

A practical computational method to predict the aerodynamic performance of two-dimensional, high-lift aerofoil configurations involves three main components: a procedure for generating suitable computational grids around the multi-element aerofoil section, the implementation of a turbulence model to predict the flow physics and an efficient solution algorithm for the mean-flow and turbulence-transport equations. Using structured grids, it is relatively straightforward to generate the highly-stretched computational cells immediately adjacent to the aerofoil surfaces which are required to resolve the boundary-layer regions in these high-Reynolds number flows. However, the turbulent boundary-layer and wake regions developing around a high-lift system can change significantly in position and thickness as the aerofoil section is pitched from small incidence angles up to and beyond the stall condition. In this situation, an unstructured-grid approach, together with flow-adaptation, may be a more efficient approach¹⁴. Also, around maximum-lift conditions, there is significant stream-wise curvature of the turbulent wakes flowing from upstream aerofoil elements over the upper surfaces of the downstream elements. The various Reynolds normal- and shear-stress components appearing in the mean-flow equations respond in different ways to the influence of flow curvature. This vector-like behaviour cannot be simulated using a scalar turbulent-viscosity coefficient to model the Reynolds stresses, as in the k- ϵ turbulence model. It is for this reason that a differential Reynolds-stress transport equation model (DRSM) is adopted in the present computational method.

2.1 Grid Generation

The unstructured grid-generation procedure used is described in detail by Marques and Johnston¹⁵ and consists of three distinct stages. Firstly, structured-like grids, consisting of directly-triangulated quadrilateral cells, are wrapped locally around the various aerofoil elements and extended downstream of the trailing edges. These anisotropic-grid regions encompass all the anticipated boundary-layer and wakes regions of the flow domain, Figure 3(a). Any overlapping cells in these regions are deleted. Next, an initial triangulation is constructed, using the Delaunay algorithm, to discretise the remaining parts of the flow domain. The final stage of the grid-generation process involves refinement of this initial Delaunay triangulation using the cell sub-division technique of Jahangirian and Johnston¹⁴. A Laplacian smoother is also applied in this region and to the outer layers of the anisotropic-grid regions, with an edge-swapping operation being used to further enhance the grid quality. The desired grid density and quality is generally achieved after 20 iterations of the cell sub-division procedure, Figure 3(b).

2.2 Governing Flow Equations

The present computational method is based on solution of the Reynolds-averaged Navier-Stokes equations applicable to two-dimensional, compressible, turbulent flow. The time-dependent, integral form of the equations is used, with steady-state solutions being obtained by time-marching procedures. The Reynolds-stress terms appearing in the governing mean-flow equations are modelled using the simplified version of the differential Reynolds-stress model of Launder, Reece and Rodi. This turbulence model solves modelled transport equations for the three Reynolds normal-stress components, the Reynolds shear stress and the rate-of-dissipation of turbulent kinetic energy. Further details concerning the mean-flow equations can be found in Johnston and Stolcis¹⁶. Cantariti and Johnston¹⁷ discuss implementation of the DRSM turbulence model which can employ either wall-function boundary conditions or a one-equation, low-Reynolds number formulation for the near-wall regions of the flow.

2.3 Solution Algorithm

The mean-flow and turbulence-transport equations are discretised in space using the cell-centred, finite-volume formulation of Jameson *et al*¹⁸, which employs additional numerical dissipation terms in order to facilitate smooth solutions. The resulting set of semi-discrete equations can be written as follows :

$$\frac{d(h_i q_i)}{dt} + R(q_i) - D(q_i) = 0 \quad (1)$$

q_i is the vector of dependent variables, R_i is the residual containing the convective, diffusive and source terms, D_i contains the numerical dissipation terms and h_i is the area of computational cell i . The equations are marched in time to a steady-state solution using an explicit, four-stage numerical scheme, with local time-stepping and implicit residual smoothing techniques being employed to enhance the convergence rate. Application of the present computational method to low-speed, high-lift configurations is described by Marques and Johnston¹⁵.

Figure 4 shows a typical convergence history of the computations, for the slat/aerofoil configuration of Run 309, and shows well-converged solutions in terms of the average density residual, lift and pressure-drag coefficients. All the computations have been run on a Samsung Q35 Laptop PC with a 2GHz Intel Core 2 CPU and 1.24GB of RAM.

3. Results

The present computational method is evaluated for transonic flows by application to three high-lift configurations, all derived from the SKF 1.1 supercritical aerofoil section. Experimental data, comprising surface static pressure distributions, are taken from tests performed in the DFVLR 1m x 1m transonic wind tunnel; Stanewsky and Thibert¹⁹ describe the wind tunnel and present experimental results for the clean SKF 1.1 aerofoil section and for the aerofoil/manoeuvre flap configuration. All the cases considered here are for a nominal free-stream Mach number of 0.6 and a Reynolds number of 2×10^6 , based on the clean aerofoil chord. The experimental data involve free transition on all aerofoil surfaces. Fixed transition points are used for all the present calculations and are measured relative to the leading edge of the clean aerofoil section. In the absence of more specific information, the nominal experimental incidence angle has been adjusted to take account of wind-tunnel wall interference effects in a rather empirical way. The procedure used is to adjust the incidence angle of the lowest-lift case for each configuration so as to match predictions with experiment for the lower surface pressure distribution on the main aerofoil section. This same incidence angle correction is then used for the subsequent higher-lift cases. The DRSM turbulence model with wall-function near-wall boundary conditions has been employed in all of the computations. Figure 5 shows the inner regions of the computational grids for the clean SKF 1.1 aerofoil section, and for this aerofoil equipped with either a trailing-edge flap or a leading-edge slat.

3.1 SKF 1.1 Aerofoil Section

The computational grid for the clean SKF 1.1 aerofoil section comprises 31,662 cells, 47,717 cell-edges and 16,096 vertices, with 342 cell-edges on the aerofoil surface. Boundary-layer transition is fixed at 0.05 and 0.4 chord lengths downstream of the leading edge on the upper and lower surfaces respectively for the computations. Two experimental cases are considered, Runs 16 and 20, and an incidence angle correction of -1.5° has been applied to the nominal experimental values. Figure 6 indicates a good level of agreement between predictions and experiment for

Run 16 which is a fully-subsonic flow condition, C_p^* being the critical pressure coefficient for sonic flow at the free-stream Mach number. The predictions for the transonic flow conditions of Run 20 are again in good agreement with experiment, Figure 7, apart from the appearance of a weak shock wave on the upper surface. This discrepancy is attributed to uncertainty in the applied corrections for wind-tunnel wall interference. The Mach number contours in Figures 6 and 7 show the development of the supersonic flow region (high speeds being indicated by yellow and the sonic line is coloured black) and the thickening of the upper-surface boundary layer (low speed being indicated by dark blue) as the incidence angle is increased between the two Runs.

3.2 SKF 1.1 Aerofoil Section with Trailing-Edge Flap

The computational grid for the SKF 1.1 aerofoil section with a manoeuvre flap deflected 15° consists of 93,485 cells, 140,597 cell-edges and 47,878 vertices. There are 371 and 252 cell-edges on the surfaces of the main-aerofoil and flap elements, respectively. Transition is fixed at 0.05 and 0.4 chord lengths on the upper and lower surfaces of the main aerofoil, respectively. Similarly, transition is fixed close to the leading edge of the flap element, at 0.85 and 0.90 chord lengths respectively on the upper and lower surfaces. Four experimental cases are considered, Runs 252 to 255, with an incidence angle correction of $-2\frac{1}{4}^\circ$ being applied to the nominal experimental values for the computations. Figures 8 to 11 indicate a very satisfactory level of agreement between predictions and experiment for the pressure distributions on the main aerofoil element and the trailing-edge flap. Note that the flap upper surface flow remains essentially subsonic for all of these flow cases. The predicted position of the main aerofoil upper surface shock wave is slightly downstream of experiment, with a small under-prediction of the pressure recovery downstream of the shock wave. Again, these differences are most probably associated with uncertainties in wind-tunnel wall interference effects. The Mach number contours show the increasing size of the supersonic region on the upper surface of the main aerofoil as the incidence angle is increased, together with an associated thickening of the main aerofoil wake above the flap upper surface. Also to be seen is the closed re-circulation bubble sitting in the flap cove region.

3.3 SKF 1.1 Aerofoil Section with Leading-Edge Slat

The computational grid for the SKF 1.1 aerofoil section equipped with a leading-edge slat deflected at an angle of 8° contains a total of 90,481 cells, 136,065 cell-edges and 46,009 vertices, with 342 cell-edges on the main aerofoil surface and 169 cell-edges on the slat element. Transition is fixed at 0.06 and 0.4 chord lengths downstream on the upper and lower surfaces of the main aerofoil, respectively. For the slat, transition is fixed at -0.06 and -0.034 chord lengths respectively on the upper and lower surfaces, the latter value being chosen to ensure a turbulent boundary layer separation at the slat hook. Four experimental cases are considered, Runs 306 to 309, with an incidence angle correction of $-3\frac{1}{4}^\circ$ being applied to the nominal experimental values for the computations. Figures 12 to 15 compare the predicted and experimental surface pressure distributions for the four cases. In general, the overall level of agreement is reasonable, with the results indicating the build-up of slat loading as the incidence angle is increased. The slat loading at a particular incidence angle tends to be over-predicted, however, which may indicate some geometric movement of the slat element in the wind tunnel tests due to the high aerodynamic loading. The Mach number contours show the development of supersonic flow regions on the slat and main aerofoil with increasing incidence angle, and the slat wake can be clearly seen passing over the upper surface of the main aerofoil.

4. Conclusions

The predictive capability of a numerical method for multi-element aerofoil, high-lift aerodynamics at transonic-flow conditions has been assessed by application to the SKF 1.1 supercritical aerofoil section in a clean configuration and equipped with either a trailing-edge flap or a leading-edge slat, employed as a transonic manoeuvre device. The computational results, using a differential Reynolds-stress turbulence model with wall-function boundary conditions, show a satisfactory level of agreement with experimental surface pressure distributions, given the uncertainties in the precise wind-tunnel wall corrections to be applied to the experimental data. Future work will involve the use of more refined near-wall computational grids, to enable the use of no-slip boundary conditions on the aerofoil surfaces rather than the semi-empirical wall-function approach adopted here. The relative utility of the two near-wall treatments can then be assessed, particularly in relation to predicting details of the shock wave/boundary layer interactions present on the upper surfaces of some aerofoil elements at these transonic flow conditions. The present computations involved the use of fixed boundary-layer transition positions, and it would be beneficial to have a transition prediction capability within the computational method.

References

- [1] Smith, A.M.O., 'High Lift Aerodynamics', *Journal of Aircraft*, Vol.12, No.6, June 1975.
- [2] Meredith, P.T., 'Viscous Phenomena Affecting High-Lift Systems and Suggestions for Future CFD Development', *High-Lift System Aerodynamics, AGARD CP-515*, Sept. 1993, pp.19-1/19-8.
- [3] Bennett, D.H. and Rousseau, W.A., 'Seven Wings the F-4 has Flown', AIAA Paper 80-3042, *AIAA Evolution of Aircraft Wing Design Symposium*, March 18, 1980.
- [4] Whitford, R., 'Fundamentals of Fighter Design', pub. Airline, 2000.
- [5] Nield, B.N., 'An Overview of the Boeing 777 High Lift Aerodynamic Design', *Aeronautical Journal*, Nov. 1995, pp. 361-371.
- [6] Caughey, D.A., 'An Inviscid Analysis of Transonic, Slatted Airfoils', AIAA Paper 74-541, 1974.
- [7] Grossman, B. and Melnik, R.E., 'The Numerical Computation of the Transonic Flow over Two-Element Airfoil Systems', *Lecture Notes in Physics*, Vol.59, 1976, pub. Springer Verlag, pp.220/227.
- [8] Arlinger, B.G., 'Analysis of Two-Element High Lift Systems in Transonic Flow', ICAS Paper 76-13, *Proceedings of 10th ICAS Congress*, 3-8 October, 1976, Ottawa, Canada, pp.125/133.
- [9] Rosch, H. and Klevenhusen, K.D., 'Flow Computation Around Multi-Element Airfoils in Viscous Transonic Flow', ICAS Paper 80-11.3, *Proceedings of 12th ICAS Congress*, 12-17 October 1980, Munich, pp.470/479.
- [10] Grossman, B. and Volpe, G., 'The Viscous Transonic Flow over Two-Element Airfoil Systems', AIAA Paper 77-688, 1977.
- [11] Leicher, S., 'Viscous Flow Simulation of High Lift Devices at Subsonic and Transonic Speed', *Computation of Viscous-Inviscid Interactions*, AGARD CP.291, 1981, 6-1/6-15.
- [12] Rumsey, C. and Ying, S., 'Prediction of High Lift: Review of Present CFD Capability', *Progress in Aerospace Sciences*, 38, 2002, pp.145-180.
- [13] Stolcis, L. and Johnston, L.J., 'Application of an Unstructured Navier-Stokes Solver to Multi-Element Airfoils Operating at Transonic Maneuver Conditions', AIAA Paper 92-2638, *10th AIAA Applied Aerodynamics Conference*, Palo Alto, California, USA, June 22-24, 1992.
- [14] Jahangirian, A. and Johnston, L.J., 'Calculation of High-Lift Aerodynamics on Adaptive Unstructured Grids', *Proceedings of 20th ICAS Congress*, 8-13 September 1996, Sorrento, Italy, Vol.2, pp.193-217, 1996.
- [15] Marques, S.P. and Johnston, L.J., 'Unstructured Grid Generation Method and Flow Solutions for Two-Dimensional, High-Lift Aerofoil Configurations', AIAA Paper 2007-1299, *45th AIAA Aerospace Sciences Meeting and Exhibit*, 8-11 January 2007, Reno, Nevada, USA.
- [16] Johnston, L.J. and Stolcis, L. 'Prediction of the High-Lift Performance of Multi-Element Aerofoils Using an Unstructured Navier-Stokes Solver', *High-Lift System Aerodynamics, AGARD CP.515*, 1993, pp.13-1/13-18.
- [17] Cantariti, F.J.-J. and Johnston, L.J., 'High-Lift Navier-Stokes Computations on Unstructured Grids Using a Differential Reynolds Stress Model', *Numerical Methods for Fluid Dynamics V*, Edited by K.W. Morton and M.J. Baines, Oxford Science Publications, 1995, pp.319/325.
- [18] Jameson, A., Baker, T.J. and Weatherill, N.P., 'Calculation of Inviscid Transonic Flow over a Complete Aircraft', AIAA Paper 86-0103, 1986.
- [19] Stanewsky, E. and Thibert, J.J., 'Airfoil SKF 1.1 with Maneuver Flap', *Experimental Data Base for Computer Program Assessment*, AGARD AR.138, 1979, pp.A5-1/A5-29.



Figure 1 Leading-Edge Slats Deployed on Dassault Rafale Aircraft

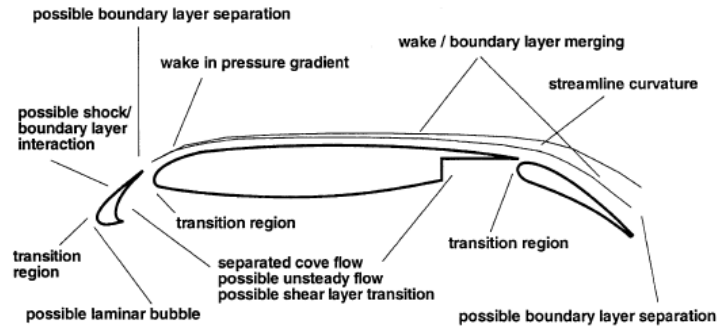


Figure 2 Flow Phenomena Present on Multi-Element, High-Lift System

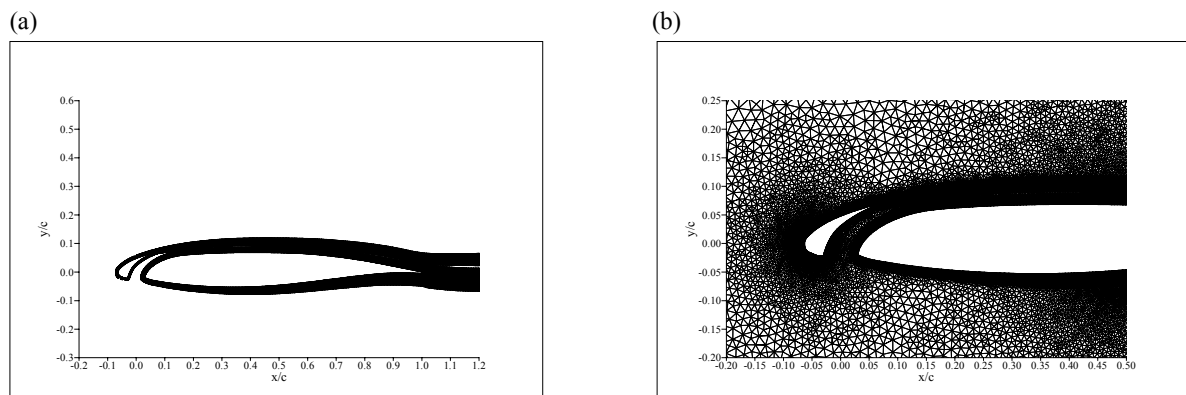


Figure 3 Details of Computational Grid for SKF 1.1 Aerofoil with Manoeuvre Slat

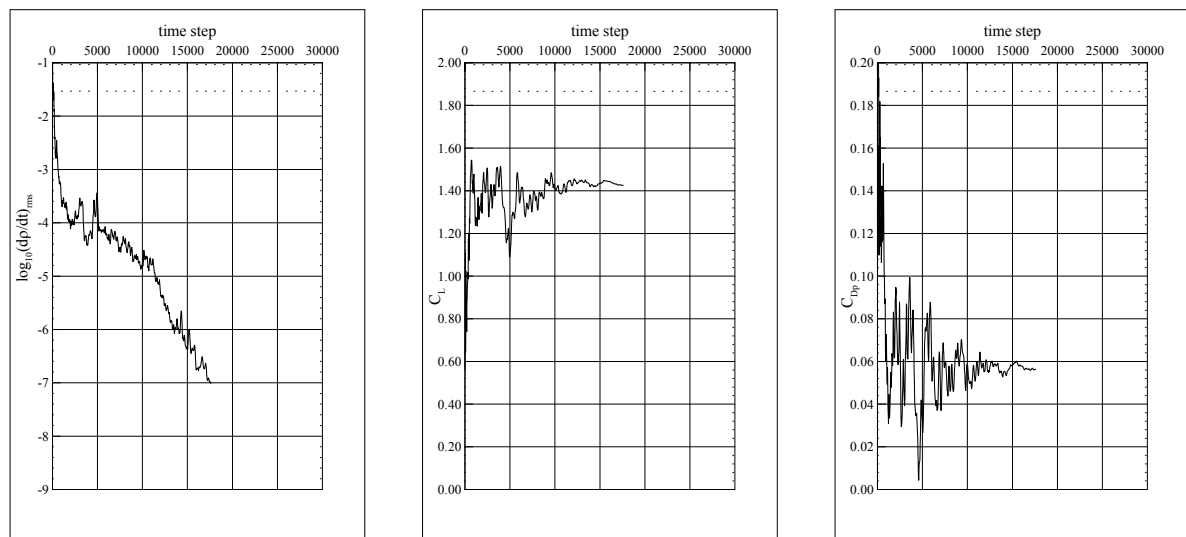


Figure 4 Convergence Histories of Density Residual, Lift and Pressure-Drag Coefficients for Run 309

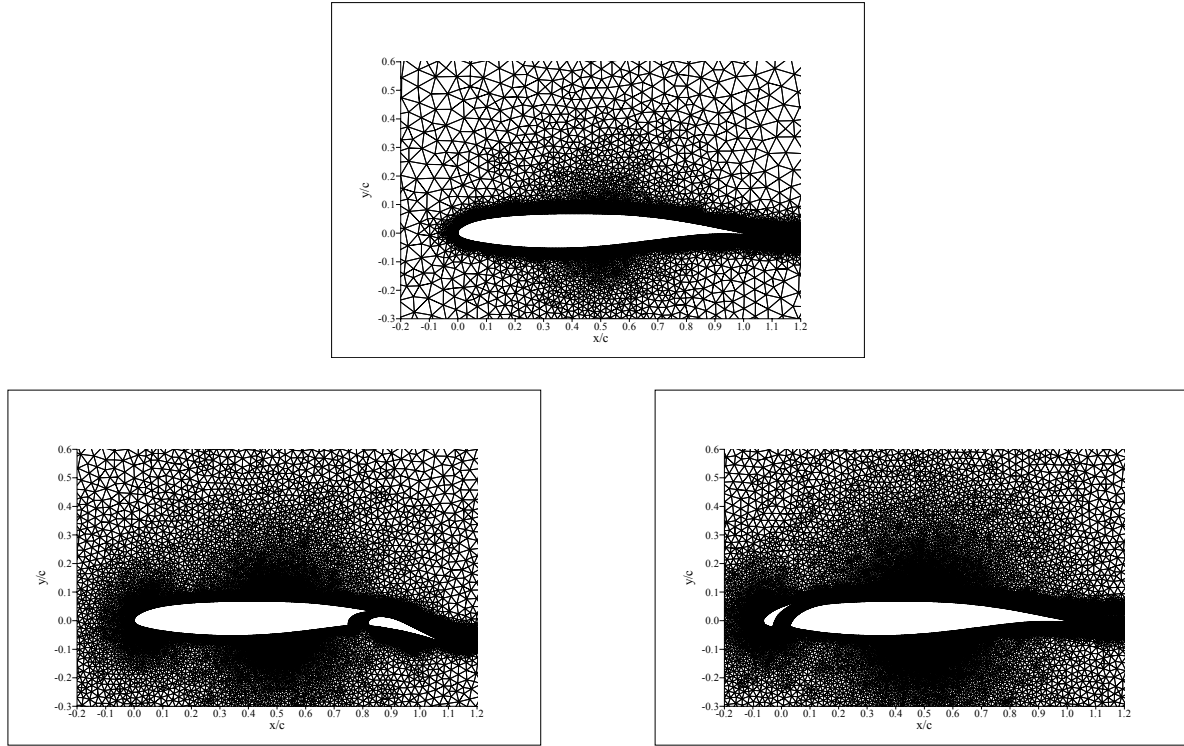


Figure 5 Computational Grids for SKF 1.1 Aerofoil Section High-Lift Configurations

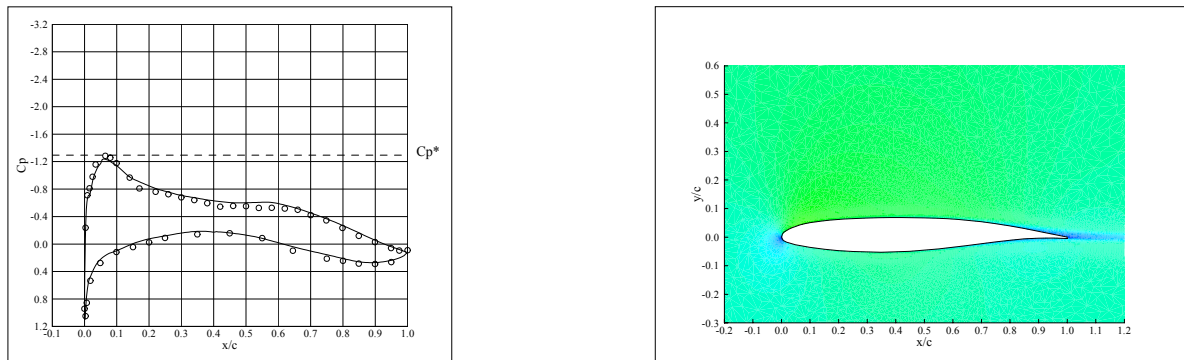


Figure 6 Surface Pressure Distribution and Mach Number Contours for Run 16, $\alpha = 2.01^\circ$

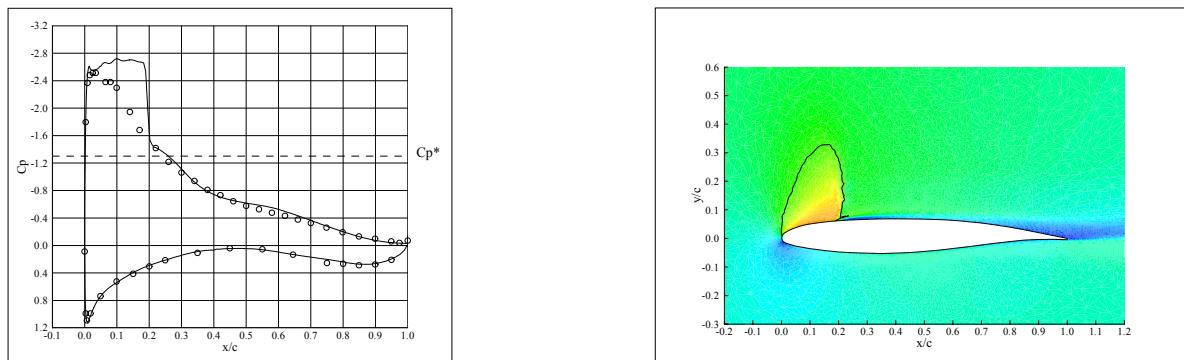


Figure 7 Surface Pressure Distribution and Mach Number Contours for Run 20, $\alpha = 7.67^\circ$

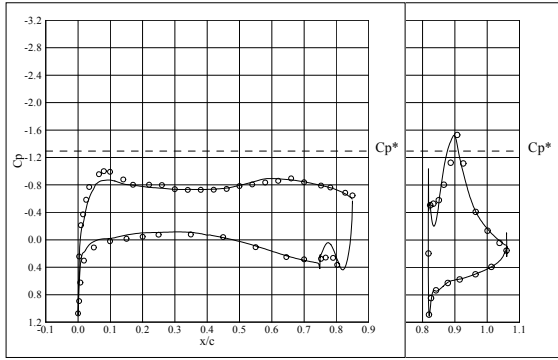


Figure 8 Surface Pressure Distribution and Mach Number Contours for Run 252, $\alpha = -3.09^\circ$

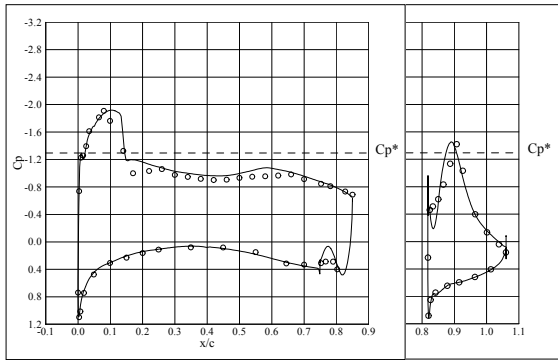
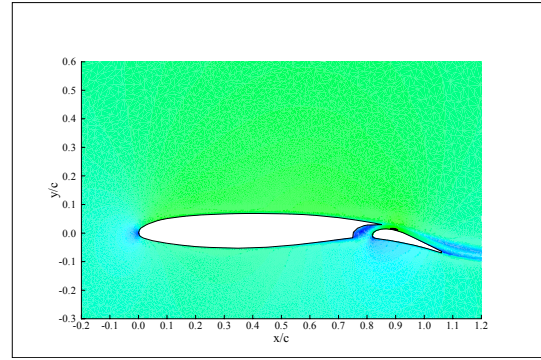


Figure 9 Surface Pressure Distribution and Mach Number Contours for Run 253, $\alpha = -0.35^\circ$

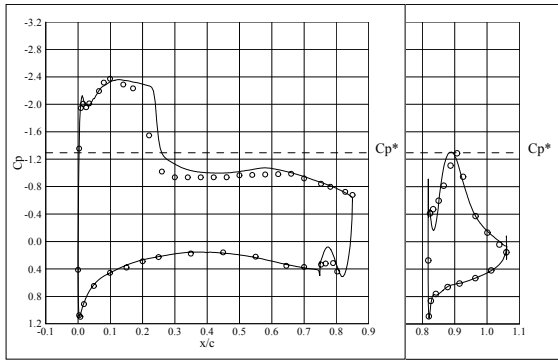
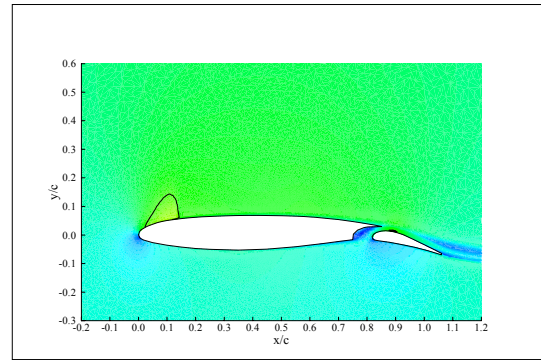


Figure 10 Surface Pressure Distribution and Mach Number Contours for Run 254, $\alpha = 1.48^\circ$

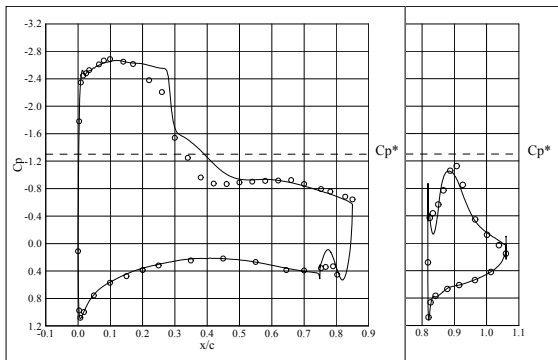
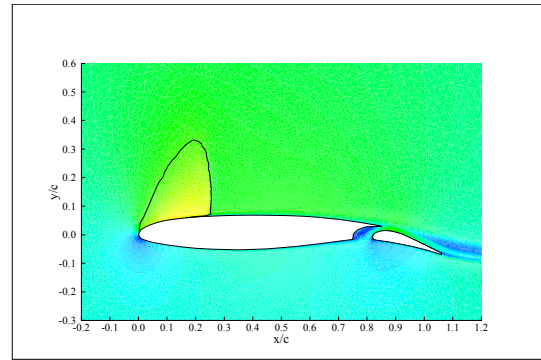
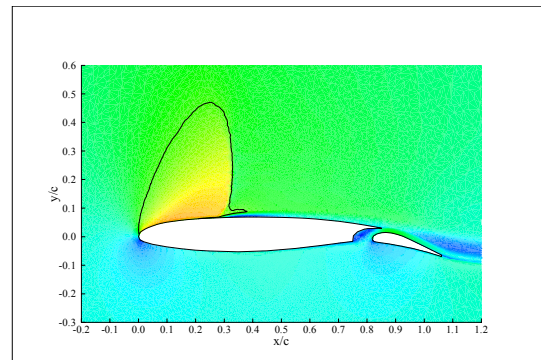


Figure 11 Surface Pressure Distribution and Mach Number Contours for Run 255, $\alpha = 3.32^\circ$



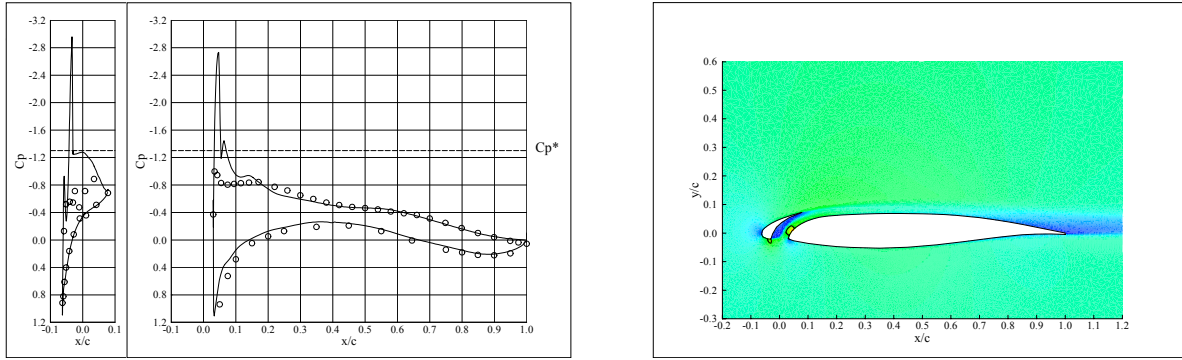


Figure 12 Surface Pressure Distribution and Mach Number Contours for Run 306, $\alpha = 1.92^\circ$

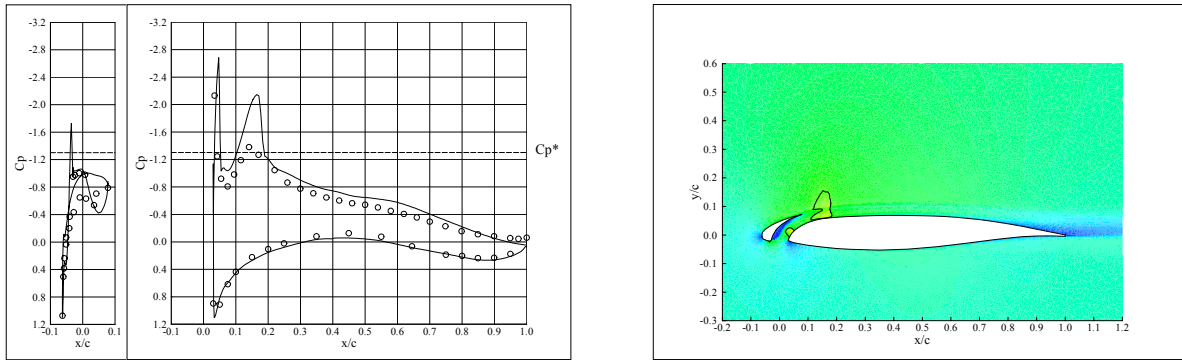


Figure 13 Surface Pressure Distribution and Mach Number Contours for Run 307, $\alpha = 4.76^\circ$

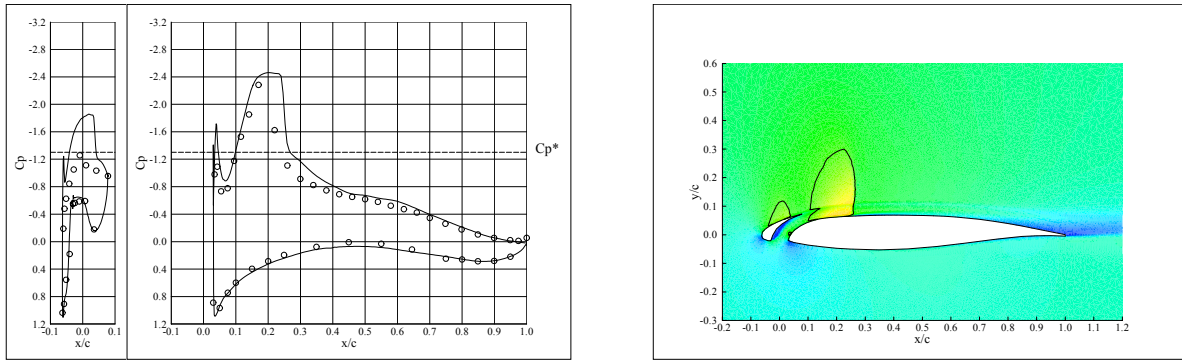


Figure 14 Surface Pressure Distribution and Mach Number Contours for Run 308, $\alpha = 7.50^\circ$

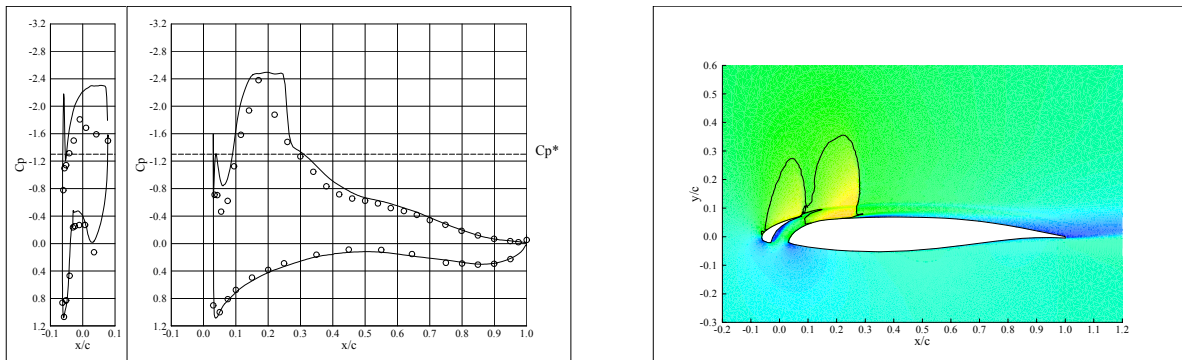


Figure 15 Surface Pressure Distribution and Mach Number Contours for Run 309, $\alpha = 9.34^\circ$